The Astrophysical Journal Letters, 710:L72–L76, 2010 February 10 doi:10.1088/2041-8205/710/1/L72

WATER VAPOR IN THE INNER 25 AU OF A YOUNG DISK AROUND A LOW-MASS PROTOSTAR*

Jes K. Jørgensen[1,4] and Ewine F. van Dishoeck[2,3]
[1] Argelander-Institut für Astronomie, University of Bonn, Auf dem Hügel 71, D-53121 Bonn, Germany; jes@snm.ku.dk
[2] Leiden Observatory, Leiden University, P.O. Box 9513, NL-2300 RA Leiden, The Netherlands; ewine@strw.leidenuniv.nl
[3] Max-Planck Institut für extraterrestrische Physik, Giessenbachstrasse, D-85748 Garching, Germany
Received 2009 October 18; accepted 2010 January 7; published 2010 January 22

ABSTRACT

Water is one of the key molecules in the physical and chemical evolution of star- and planet-forming regions. We here report the first spatially resolved observation of thermal emission of (an isotopologue of) water with the Plateau de Bure Interferometer toward the deeply embedded Class 0 protostar NGC 1333-IRAS4B. The observations of the $H_2^{18}O$ $3_{1,3}$–$2_{2,0}$ transition at 203.4 GHz resolve the emission of water toward this source with an extent of about 0.″2 corresponding to the inner 25 AU (radius). The $H_2^{18}O$ emission reveals a tentative velocity gradient perpendicular to the extent of the protostellar outflow/jet probed by observations of CO rotational transitions and water masers. The line is narrow, ≈1 km s^{-1} (FWHM), significantly less than what would be expected for emission from an infalling envelope or accretion shock, but consistent with emission from a disk seen at a low inclination angle. The water column density inferred from these data suggests that the water emitting gas is a thin warm layer containing about 25 $M_{\rm Earth}$ of material, 0.03% of the total disk mass traced by continuum observations.

Key words: astrochemistry – ISM: abundances – ISM: individual objects (NGC 1333-IRAS4B) – protoplanetary disks – stars: formation

1. INTRODUCTION

Water is one of the most important molecules in star-forming regions: it is a dominant form of oxygen, is important in the energy balance, and is *ultimately* associated with the formation of planets and emergence of life. Thus, following the water "trail" from collapsing clouds to protoplanetary disks is a fundamental problem in astronomy and astrochemistry. In the cold and quiescent regions, the gaseous water abundance is low, only 10^{-9}–10^{-8} (e.g., Bergin & Snell 2002), but in regions with intense heating or active shocks, its abundance can reach 10^{-4} with respect to H_2—comparable to or higher than that of CO (e.g., Harwit et al. 1998). Which mechanism is most important for regulating the H_2O abundance in low-mass protostars is still heavily debated. Is it passive heating of the collapsing envelope by the accretion luminosity from forming stars (e.g., Ceccarelli et al. 1998; Maret et al. 2002), or shocks either caused by protostellar outflows (e.g., Nisini et al. 1999) or related to ongoing accretion onto circumstellar disks (Watson et al. 2007)? H_2O is also a key molecule in the chemistry in regions of star formation: in large parts of the cold and dense envelopes around low-mass protostars, H_2O is the dominant constituent of the icy mantles of dust grains (e.g., Whittet et al. 1988; Boogert et al. 2008). Its evaporation at temperatures higher than 90–100 K determines at what point water itself and any complex organic molecules, formed in these ice mantles, are injected into the gas phase.

This discussion has received new fuel with the detection of surprisingly strong highly excited H_2O lines at mid-infrared wavelengths with the *Spitzer Space Telescope*'s infrared spectrograph (IRS) toward one deeply embedded Class 0 protostar, NGC 1333-IRAS4B, by Watson et al. (2007). Based on the high critical density of the observed lines and temperature (∼170 K), Watson et al. argue that the water emission observed toward this source has its origin in an accretion shock in its circumstellar disk. Those data could not spatially or spectrally resolve the water emission, however.

In this Letter, we present observations at 203 GHz of the $H_2^{18}O$ isotopologue at high angular resolution (0.″5) using the Institut de Radioastronomie Millimétrique (IRAM) Plateau de Bure Interferometer (PdBI) to determine the origin of water emission in low-mass protostars. This isotopic line is a useful tracer of H_2O as it can be detected and imaged at high angular resolution from the ground under good weather conditions (e.g., Jacq et al. 1988; Gensheimer et al. 1996; van der Tak et al. 2006). Its upper level energy of 203.6 K is well matched to the observed excitation temperature of water seen by *Spitzer*.

2. OBSERVATIONS

We observed NGC 1333-IRAS4B (hereafter IRAS4B; $\alpha = 03^{\rm h}29^{\rm m}12^{\rm s}.00$, $\delta = +31^\circ13'08''.1$ [J2000] Jørgensen et al. 2007b)[5] using the six-element IRAM PdBI. The receivers were tuned to the para-$H_2^{18}O$ $3_{1,3}$–$2_{2,0}$ transition at 203.407498 GHz (1.47 mm). The correlator was set up with one unit with a bandwidth of 36 MHz (53 km s^{-1}) centered on this frequency providing a spectral resolution on 460 channels of 0.078 MHz (0.11 km s^{-1}). The source was observed in two configurations: in the C configuration on 2008 December 2 and in the B configuration on 2009 January 11 and 13. About 11 hr were spent in each configuration (including time used on gain calibrators etc.). When combined, these two configurations cover baselines with lengths from 17.8 to 452 m (12 to 308 kλ).

The data were calibrated and imaged using the CLIC and MAPPING packages from the IRAM GILDAS software. The calibration followed the standard approach: the absolute flux calibration was established through observations of MWC 349, the bandpass by observations of the strong quasar 3c454.3 and

* Based on observations carried out with the Institut de Radioastronomie Millimétrique (IRAM) Plateau de Bure Interferometer. IRAM is supported by INSU/CNRS (France), MPG (Germany), and IGN (Spain).
[4] Current address: Centre for Star and Planet Formation, Natural History Museum of Denmark, University of Copenhagen, Øster Voldgade 5-7, DK-1350 Copenhagen K, Denmark.

[5] In this Letter, we adopt a distance of 250 pc for NGC 1333-IRAS4B (see the discussion in Enoch et al. 2006).

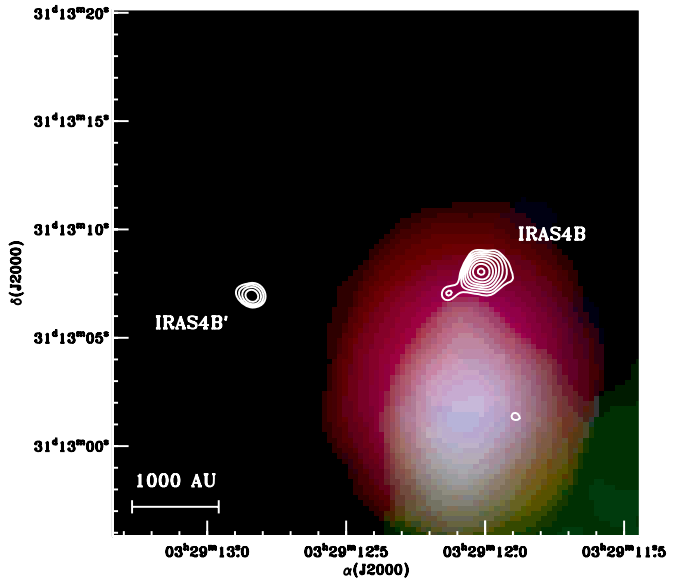

Figure 1. Continuum image of IRAS4B and IRAS4B′ from the IRAM PdBI observations (contours shown in logarithmic steps from 0.015 to 0.25 Jy beam^{-1} overlaid on the *Spitzer Space Telescope* mid-infrared image (Jørgensen et al. 2006; Gutermuth et al. 2008) with 4.5 μm emission shown in blue, 8.0 μm in green, and 24 μm in red.

Table 1
Parameters for IRAS4B and IRAS4B′ from Elliptical Gaussian Fits to Their Continuum Emission

Parameter	IRAS4B	IRAS4B′
Flux	0.586 Jy	0.128 Jy
R.A. (J2000)	03:29:12.01	03:29:12.84
Decl. (J2000)	31:13:08.07	31:13:06.93
Extent[a]	0.″80 × 0.″54 (−65°)	0.″56 × 0.″45 (−86°)

Note. [a] Size of Gaussian from fit in the (u, v) plane (i.e., deconvolved full width at half-maximum (FWHM) size) and position angle of major axes (in parentheses).

the complex gains by regular observations of the nearby quasar J0336+323 (approximately 0.8 Jy at 1.45 mm). Integrations with clearly deviating amplitudes and/or phases were flagged, and the continuum was subtracted prior to Fourier transformation of the line data. With natural weighting, the resulting beam size is 0.″67 × 0.″55 at a position angle of 36.°7; the field of view is 25″ (half-power beamwidth) at 1.45 mm. The resulting rms noise level is 11 mJy beam^{-1} channel^{-1} for the line data using natural weighting. The continuum sensitivity is limited by the dynamical range of the interferometer and the resulting rms noise level is a few mJy beam^{-1}.

3. RESULTS

Figure 1 shows the continuum image of the observed region around IRAS4B. As seen, both IRAS4B and its nearby companion IRAS4B′ are clearly detected in the image. Table 1 lists the results of elliptical Gaussian fits to the two sources: both are resolved with fluxes in agreement with the results from Jørgensen et al. (2007b) assuming that it has its origin in thermal dust continuum emission with $F_\nu \propto \nu^\alpha$ with $\alpha \approx 2.5$–3. The continuum peak is clearly offset by 5″–7″ from the emission at 3.6–24 μm seen in the *Spitzer Space Telescope* images of IRAS4B; an indication that the *Spitzer* emission has its origin in material heated by the protostellar outflow even at 24 μm (see also Jørgensen et al. 2007a, and Figure 2 of Allen et al. 2007).

Figure 2 shows the spectrum toward the continuum peak of IRAS4B. A number of lines are clearly detected as listed in Table 2—including the targeted $H_2^{18}O$ $3_{1,3}$–$2_{2,0}$ line. For the line identification, we used the JPL (Pickett et al. 1998) and CDMS (Müller et al. 2001, 2005) databases and cross-checked those with the online Splatalogue compilation. Since all of the lines are narrow, little line-blending occurs, in contrast to high-mass star-forming regions. Also, all the assigned lines are centered within 0.1–0.2 km s^{-1} of the systemic velocity of 7.0 km s^{-1} of IRAS4B. Most prominent in the spectrum are lines of dimethyl ether, CH_3OCH_3, with five identified transitions. In addition, lines of sulfur dioxide, SO_2, and water, $H_2^{18}O$, are

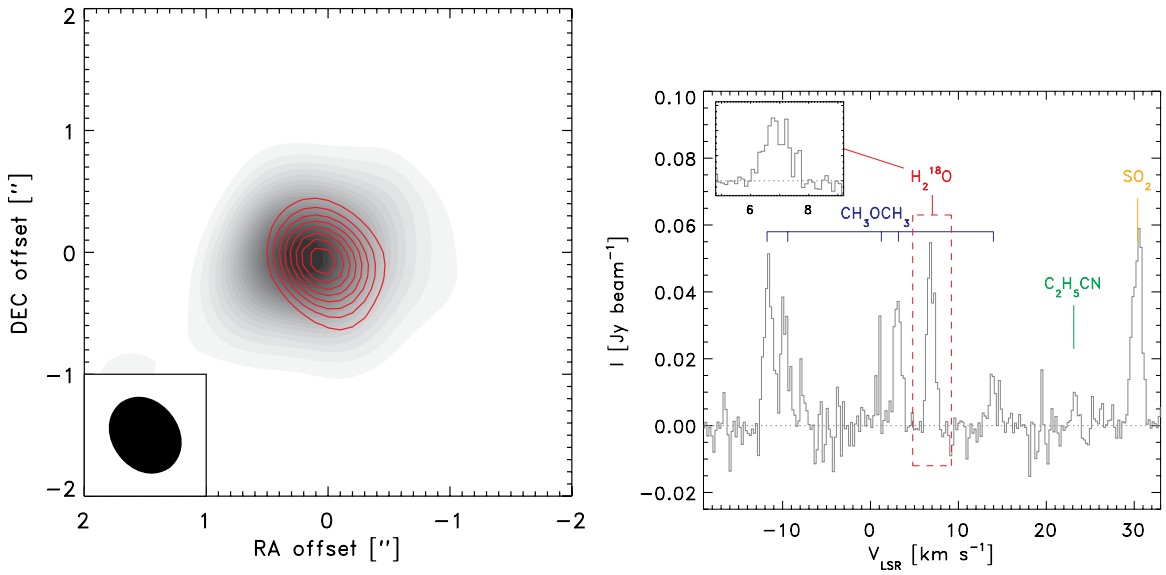

Figure 2. Left: integrated emission of the $H_2^{18}O$ line (contours in steps of 5 mJy beam^{-1} km s^{-1} starting at 10 mJy beam^{-1} km s^{-1}) plotted over the continuum emission (gray scale). Right: spectrum extracted in the central 0.″6 × 0.″5 beam toward the continuum position for IRAS4B. The detected lines are indicated at the position of their catalog rest frequency corrected for the 7.0 km s^{-1} systemic velocity of IRAS4B. The spectrum has been binned to twice the observed resolution. The inset shows a blow-up of the $H_2^{18}O$ line at the original resolution.

Table 2
Identified Lines and Results from Gaussian Fit to Emission in the (u, v) Plane

Molecule	Transition	Frequency (GHz)	E_u (K)	$\mu^2 S$	Flux[a] (Jy km s^{-1})	Offset ($\Delta\alpha$, $\Delta\delta$)[b] ($''$)	Size[c] ($''$)
$H_2^{18}O$	$3_{1,3}$–$2_{2,0}$	203.407498	203.7	0.344	0.081	(−0.11; −0.02)	0.″20
CH_3OCH_3	$3_{3,1}$–$2_{2,1}$ EA	203.402779	18.12	9.29	0.035	(−0.14; −0.07)	0.″48
	$3_{3,1}$–$2_{2,1}$ EE	203.410112	18.12	31.1	0.088	(−0.14; −0.02)	0.″46
	$3_{3,0}$–$2_{2,1}$ AE	203.411431	18.12	20.0	0.044	(−0.12; −0.02)	0.″31
	$3_{3,0}$–$2_{2,1}$ AA	203.418656	18.12	33.4	0.12	(−0.12; +0.03)	0.″67
	$3_{3,0}$–$2_{2,1}$ EE	203.420253	18.12	22.3	0.094	(−0.16; +0.00)	0.″25
C_2H_5CN	$23_{2,22}$–$22_{2,21}$	203.396581	122.3	338	0.045	(+0.02; +0.00)	0.″37
SO_2	$12_{0,12}$–$11_{1,11}$	203.391550[d]	70.12	22.5	0.12	(−0.11; −0.02)	0.″41

Notes.
[a] Total flux from fitting circular Gaussian to integrated line emission in the (u, v) plane. For conversion to brightness temperatures, the gain of the interferometric observations with the current beam size is 0.0126 Jy K^{-1}—i.e., implying an integrated line strength for the $H_2^{18}O$ line of 6.5 K km s^{-1}.
[b] Peak offset with respect to the continuum peak estimated from the Gaussian fit.
[c] Extent of emission (FWHM) from the Gaussian fit.
[d] Catalog frequency uncertain (accuracy ±0.1 MHz). The observed SO_2 peak indicates a frequency higher by 0.1 MHz than the tabulated one.

clear detections with a fainter line of ethyl cyanide, C_2H_5CN, also present. Concerning the confidence of the assignment of the $H_2^{18}O$ line, according to the Splatalogue compilation no other transitions fall within ±1 km s^{-1} of the location of the $H_2^{18}O$ line. Offsets by 1–2 km s^{-1} are transitions of $^{13}CH_2CHCN$, $^{13}CH_3CH_2CN$, and $(CH_3)_2CO$: the two former can be ruled out because of the lack of additional components which should have been observable at larger velocity offsets, whereas the latter has a very low intrinsic line strength.

For each of the detected lines we fit a circular Gaussian in the (u, v) plane to the line emission integrated over the widths of the lines to zero intensity (about ±1 km s^{-1}). The derived fluxes, peak positions and sizes are given in Table 2 as well. All the detected lines are marginally resolved with deconvolved sizes of 0.″2–0.″6, corresponding to radii of only 25–75 AU. Interestingly, most of the detected lines are offset by about 0.″10–0.″15 from the continuum position in right ascension (R.A.)—with the exception of C_2H_5CN. The peaks of the molecular emission still fall within the deconvolved extent of the continuum emission, though. The images of the complex organic molecules and SO_2 will be discussed elsewhere.

4. DISCUSSION

4.1. Velocity Field

The high spectral and spatial resolution offered by the IRAM data reveals a tentative velocity gradient in the $H_2^{18}O$ emission. Figure 3 shows a moment-1 (velocity) map of this emission indicating a change in velocity of a few ×0.1 km s^{-1} over the extent of the source emission. To estimate the magnitude of the velocity gradient, the centroid of the emission was determined channel by channel in the (u, v) plane. The derived offsets along and perpendicular to the largest velocity gradient are then plotted as a function of velocity and a linear fit performed (Figure 3). The velocity gradient found in this way is 9.4 km s^{-1} arcsec^{-1} or 7.7 × 10^3 km s^{-1}pc^{-1} at a 3.5σ–4σ confidence level. The velocity gradient is about three orders of magnitude larger than the typical gradients observed on arcminute scales in pre-stellar cores (Goodman et al. 1993)—supporting a scenario in which the $H_2^{18}O$ emission has its origin in a more rapidly rotating structure such as a central disk—although it is not possible to address whether the velocity, for example, is Keplerian in nature. The position angle of the largest gradient is ≈75° measured east of north (with an accuracy of ±5°–10° from the gradient measured in the (u, v) plane), which, interestingly, is nearly perpendicular to the axis of the protostellar outflow (upper panel of Figure 3) traced by water masers in the north–south direction with a position angle of −29° (Marvel et al. 2008; Desmurs et al. 2009) and thermal line emission on larger scales at a position angle of 0° (e.g., Choi 2001; Jørgensen et al. 2007b).

Besides the tentative velocity gradient, the $H_2^{18}O$ line width is remarkably narrow: its width to zero intensity is about 1.7 km s^{-1} with a FWHM from a Gaussian fit of 1.0 km s^{-1}. For comparison, a free-falling envelope toward a central star with even a very small mass of 0.1 $M_\odot$ would have a characteristic infall velocity of 2.5 km s^{-1} at 25 AU—i.e., we would expect a line width significantly larger than that observed in this case. A rotationally supported edge-on disk would show a similar line width, whereas a more face-on disk would provide a lower width in agreement with what is observed, although a disk seen entirely face-on would not produce any observable velocity gradient. Alternatively, an inclined disk with sub-Keplerian rotation (e.g., a "pseudo-disk;" Galli & Shu 1993; Hennebelle & Ciardi 2009) or a density enhancement in the inner envelope due to a magnetic shock wall slowing down the infalling material (Tassis & Mouschovias 2005; Chiang et al. 2008) could result in a lower line width—although such phenomena usually occur on larger scales than 25 AU. Watson et al. (2007) argued based on the detected mid-IR emission that the outflow cone must be close to pole-on providing a low-opacity route for the IR emission to escape toward the observer. This would imply a nearly face-on disk. However, the proper motions and radial velocities of H_2O masers suggest an outflow directed closer to the plane of the sky (Marvel et al. 2008; Desmurs et al. 2009). Clearly, observations of the dynamical structure of the inner regions of IRAS4B with even higher angular resolution are required to distinguish between these scenarios.

4.2. Column Density, Mass, and Abundance

The strength of the $H_2^{18}O$ transition suggests a significant reservoir of water vapor toward IRAS4B. We estimate the column density of H_2O by adopting an excitation temperature for p-$H_2^{18}O$ of 170 K from the modeling results of Watson

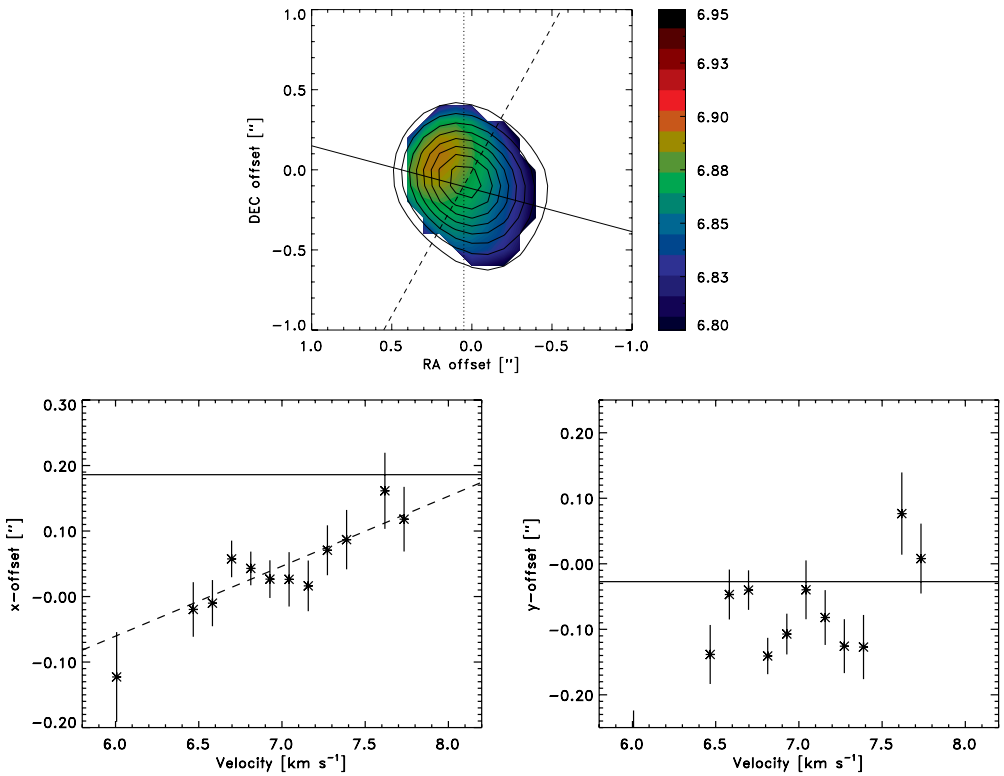

Figure 3. Velocity gradient in the $H_2^{18}O$ emission toward IRAS4B: Upper panel: moment-1 (velocity) map with the direction of the largest gradient indicated by the solid line and the direction of the water masers with the dashed line, and the larger-scale molecular outflow with the dotted line. Lower panels: the fitted position offset (relative to the phase center of the observations) along (left) and perpendicular (right) to the direction of the main gradient for each channel where at least 3σ emission is detected. The solid lines in both panels indicate the continuum position; the dashed line in the left panel a linear gradient fit to the data.

et al. (2007) and assume that the emission is optically thin and uniform over its extent. With these assumptions, we estimate a column density for p-$H_2^{18}O$ of 4×10^{15} cm^{-2}, which translates into a total H_2O column density of 9×10^{18} cm^{-2} assuming a $^{16}O/^{18}O$ ratio of 560 and an ortho–para ratio for H_2O of 3 (i.e., an ortho–para ratio established at high temperatures). For comparison, the column density estimated based on the *Spitzer* detections by Watson et al. (2007) is two orders of magnitude lower, 9.2×10^{16} cm^{-2}, over an emitting area of $0\farcs24 \times 0\farcs24$—i.e., comparable to the deconvolved size of the $H_2^{18}O$ emission here. Our inferred column density is almost unchanged if the excitation temperature is lowered to 100 K and increases by up to a factor 5 if the temperature is increased to 1000 K. These temperatures cover the range of conditions expected for any of the scenarios for the origin of the H_2O emission discussed in Section 1.

The total mass contained in the detected H_2O is $6.0 \times 10^{-8}\ M_\odot$, or 0.02 $M_{\rm Earth}$. Assuming a typical H_2O abundance relative to H_2 of 10^{-4}, corresponding to sublimation of the H_2O-rich dust ice mantles (e.g., Pontoppidan et al. 2004), the total H_2 mass of the H_2O-emitting material (dust+gas) is $7.5 \times 10^{-5}\ M_\odot$ or 25 $M_{\rm Earth}$. For comparison, the mass of the compact disk around IRAS4B inferred from the modeling of high angular resolution dust continuum observations is $0.24\ M_\odot$ (Jørgensen et al. 2009). Thus, if the $H_2^{18}O$ emission has its origin in this disk, it arises in a small fraction $\approx$0.03% of the material in the disk.

Alternatively, in the absence of such a disk, it is possible that the emission has its origin in the hot inner region of the protostellar envelope where the temperature is $\gtrsim$100 K: for a simple power-law envelope density profile reproducing the sub-millimeter continuum emission for IRAS4B on scales larger than $\sim$1000 AU ($2.8\ M_\odot$ within 8000 AU; Jørgensen et al. 2009), the mass within 25 AU (where the temperature is higher than about 100 K) is about $5 \times 10^{-4}\ M_\odot$, implying a H_2O abundance of about 1.5×10^{-5}. However, such a model is not self-consistent on small scales: to fit the observed compact dust continuum emission seen by the interferometer a strong increase in the envelope density on small scales by two orders of magnitude is required—above the already increasing radial density profile (e.g., Jørgensen et al. 2009). However, if such a density enhancement was due to a magnetic field wall as discussed above (Chiang et al. 2008), the H_2O abundance would be lower by the same amount, dropping to about 1.5×10^{-7}. This abundance is low compared to the expectation from the full desorption of the H_2O mantles and also lower than the constraints on the H_2O abundance in the outer envelopes of the IRAS4 sources where H_2O is frozen out based on ISO-LWS results (Maret et al. 2002). A low H_2O abundance in the region of grain–mantle desorption may reflect destruction of H_2O by X-rays (Stäuber et al. 2006), but the H_2O abundance would need to be reduced to the levels of the outer cold envelope where H_2O is frozen out and thus could not provide the compact emission observed here.

Models of the chemistry in more evolved disks around pre-main-sequence stars (where the envelope has dissipated) show a warm upper layer where H_2O gas can exist. Although these models are not fully appropriate for disks in the embedded phase, where UV photons may not be able to freely reach the disk surface and heat the gas, they provide a useful reference point for comparison. If the H_2O gas-phase abundance is just determined by the balance of photodesorption of H_2O ice and

freeze-out, typical gaseous H_2O column densities at 10–25 AU are a few $\times 10^{18}$ cm^{-2}, dropping rapidly at larger radii in these models (e.g., Öberg et al. 2009), only slightly lower than those found here. Alternatively, the temperatures in the upper layers of the disk may be hot enough to drive an active gas-phase chemistry. Woitke et al. (2009) find a layer of irradiated hot water at altitudes $z/R = 0.1$–0.3 extending out to 30 AU where temperatures are 200–1500 K and densities are 10^8–10^{10} cm^{-3}, comparable to the conditions deduced here (see also Glassgold et al. 2009). The H_2O mass in this layer is $\sim 10^{-4} M_{\rm Earth}$ in their model, about two orders of magnitude lower than that derived on basis of the $H_2^{18}O$ observations presented in this Letter. Because their H_2O/H_2 abundance is only 10^{-6}–10^{-5}, the inferred total warm H_2 mass is comparable.

The discrepancy between the column densities from these data and those from the *Spitzer* mid-infrared observations (Watson et al. 2007) remains significant, though. A possible explanation is that the mid-infrared observations are limited by extinction and thus do not probe the total water column density. Alternatively, a lower temperature of the H_2O emitting gas of $\sim$100 K could with an unchanged column density keep the observed $H_2^{18}O$ line intensity at the same level while decreasing the mid-IR line flux predicted by the model.

It also remains a question why IRAS4B is the only source with strong H_2O lines at mid-infrared wavelengths (Watson et al. 2007). Watson et al. proposed that IRAS4B was either seen in a particularly favorable geometry—with the H_2O mid-infrared emission from disks around other sources being masked by optically thick envelopes—or that the release of H_2O into the gas phase constituted a particularly short-lived stage in the evolution of embedded protostars. These scenarios could easily be distinguished by further observations of $H_2^{18}O$ emission from embedded protostars at (sub)millimeter wavelengths where the envelopes are optically thin, and water should thus be detectable if present at similar levels as in IRAS4B. Future observations with the Atacama Large Millimeter Array in Band 5 will fully open this topic up for ground-based observations of large samples of embedded protostars in the same lines.

We are grateful to the IRAM staff—Arancha Castro-Carrizo, in particular—for help with the observations and reduction of the resulting data, and to Michiel Hogerheijde and Ruud Visser for information on H_2O gas-phase column densities in disk models. We are also grateful to David Neufeld and the anonymous referee for insightful comments on the Letter. The research in astrochemistry in Leiden is supported by a Spinoza Grant from the Netherlands Organization for Scientific Research (NWO) and a NOVA grant.

REFERENCES

Allen, L., et al. 2007, in Protostars and Planets V, ed. B. Reipurth, D. Jewitt, & K. Keil (Tucson, AZ: Univ. Arizona Press), 361
Bergin, E. A., & Snell, R. L. 2002, ApJ, 581, L105
Boogert, A. C. A., et al. 2008, ApJ, 678, 985
Ceccarelli, C., et al. 1998, A&A, 331, 372
Chiang, H.-F., Looney, L. W., Tassis, K., Mundy, L. G., & Mouschovias, T. C. 2008, ApJ, 680, 474
Choi, M. 2001, ApJ, 553, 219
Desmurs, J., Codella, C., Santiago-García, J., Tafalla, M., & Bachiller, R. 2009, A&A, 498, 753
Enoch, M. L., et al. 2006, ApJ, 638, 293
Galli, D., & Shu, F. H. 1993, ApJ, 417, 220
Gensheimer, P. D., Mauersberger, R., & Wilson, T. L. 1996, A&A, 314, 281
Glassgold, A. E., Meijerink, R., & Najita, J. R. 2009, ApJ, 701, 142
Goodman, A. A., Benson, P. J., Fuller, G. A., & Myers, P. C. 1993, ApJ, 406, 528
Gutermuth, R. A., et al. 2008, ApJ, 674, 336
Harwit, M., Neufeld, D. A., Melnick, G. J., & Kaufman, M. J. 1998, ApJ, 497, L105
Hennebelle, P., & Ciardi, A. 2009, A&A, 506, L29
Jacq, T., Henkel, C., Walmsley, C. M., Jewell, P. R., & Baudry, A. 1988, A&A, 199, L5
Jørgensen, J. K., Johnstone, D., Kirk, H., & Myers, P. C. 2007a, ApJ, 656, 293
Jørgensen, J. K., van Dishoeck, E. F., Visser, R., Bourke, T. L., Wilner, D. J., Lommen, D., Hogerheijde, M. R., & Myers, P. C. 2009, A&A, 507, 861
Jørgensen, J. K., et al. 2006, ApJ, 645, 1246
Jørgensen, J. K., et al. 2007b, ApJ, 659, 479
Maret, S., Ceccarelli, C., Caux, E., Tielens, A. G. G. M., & Castets, A. 2002, A&A, 395, 573
Marvel, K. B., Wilking, B. A., Claussen, M. J., & Wootten, A. 2008, ApJ, 685, 285
Müller, H. S. P., Schlöder, F., Stutzki, J., & Winnewisser, G. 2005, J. Mol. Struct., 742, 215
Müller, H. S. P., Thorwirth, S., Roth, D. A., & Winnewisser, G. 2001, A&A, 370, L49
Nisini, B., et al. 1999, A&A, 350, 529
Öberg, K. I., Linnartz, H., Visser, R., & van Dishoeck, E. F. 2009, ApJ, 693, 1209
Pickett, H. M., Poynter, I. R. L., Cohen, E. A., Delitsky, M. L., Pearson, J. C., & Muller, H. S. P. 1998, J. Quant. Spectrosc. Radiat. Transfer, 60, 883
Pontoppidan, K. M., van Dishoeck, E. F., & Dartois, E. 2004, A&A, 426, 925
Stäuber, P., Jørgensen, J. K., van Dishoeck, E. F., Doty, S. D., & Benz, A. O. 2006, A&A, 453, 555
Tassis, K., & Mouschovias, T. C. 2005, ApJ, 618, 783
van der Tak, F. F. S., Walmsley, C. M., Herpin, F., & Ceccarelli, C. 2006, A&A, 447, 1011
Watson, D. M., et al. 2007, Nature, 448, 1026
Whittet, D. C. B., Bode, M. F., Longmore, A. J., Adamson, A. J., McFadzean, A. D., Aitken, D. K., & Roche, P. F. 1988, MNRAS, 233, 321
Woitke, P., Thi, W., Kamp, I., & Hogerheijde, M. R. 2009, A&A, 501, L5